Signal Processing 91 (2011) 1275–1283

Contents lists available at ScienceDirect

Signal Processing

journal homepage: www.elsevier.com/locate/sigpro

Blood velocity estimation using ultrasound and spectral iterative adaptive approaches ☆

Erik Gudmundson [a,b,*], Andreas Jakobsson [a], Jørgen A. Jensen [c], Petre Stoica [d]

[a] Department of Mathematical Statistics, Lund University, P.O. Box 118, SE-221 00 Lund, Sweden
[b] Signal Processing Lab, ACCESS Linnaeus Center, KTH - Royal Institute of Technology, SE-100 44 Stockholm, Sweden
[c] Center for Fast Ultrasound Imaging, Department of Electrical Engineering, Technical University of Denmark, DK-2800 Kgs. Lyngby, Denmark
[d] Department of Information Technology, Uppsala University, P.O. Box 337, SE-751 05 Uppsala, Sweden

ARTICLE INFO

Article history:
Received 11 February 2010
Received in revised form
3 September 2010
Accepted 26 December 2010
Available online 30 December 2010

Keywords:
Irregular sampling
Blood velocity estimation
Medical ultrasound
Spectral estimation

ABSTRACT

This paper proposes two novel iterative data-adaptive spectral estimation techniques for blood velocity estimation using medical ultrasound scanners. The techniques make no assumption on the sampling pattern of the emissions or the depth samples, allowing for duplex mode transmissions where B-mode images are interleaved with the Doppler emissions. Furthermore, the techniques are shown, using both simplified and more realistic Field II simulations as well as *in vivo* data, to outperform current state-of-the-art techniques, allowing for accurate estimation of the blood velocity spectrum using only 30% of the transmissions, thereby allowing for the examination of two separate vessel regions while retaining an adequate updating rate of the B-mode images. In addition, the proposed methods also allow for more flexible transmission patterns, as well as exhibit fewer spectral artifacts as compared to earlier techniques.

© 2011 Elsevier B.V. All rights reserved.

1. Introduction

In medical ultrasound systems, spectral Doppler is a powerful tool for non-invasive estimation of velocities in blood vessels (see, e.g., [1] and the references therein). The data for the estimation is created by focusing the ultrasound transducer array along a single direction and sampling data at the depth of interest. The velocity of the moving blood can be estimated by illuminating the same image line repeatedly, and hereby follow the motion of the blood. Taking out a single sample from each pulse emission produces a signal sampled at the pulse repetition frequency, f_{prf}, which yields a sinusoidal signal with a frequency of

$$f_p = \frac{2v_z}{c} f_c, \tag{1}$$

where v_z is the blood velocity along the ultrasound direction, c=1540 m/s is the speed of propagation, and f_c the emitted ultrasound (center) frequency (typically 3–10 MHz) [1]. A common way of estimating the blood velocity at a specific depth is to estimate the power spectral density (PSD) of the sampled signal. Displaying the PSD as a function of time, a so-called sono- or spectrogram, visualizes changes in the blood velocity distribution over time. Traditionally, in ultrasound imaging, the PSD is estimated using the periodogram or an averaged periodogram, also known as Welch's method [2]. However, as is well-known, this approach suffers from low resolution and/or high leakage, and to achieve sufficient spectral resolution, the duration of the observation window must be long (see, e.g., [2]). This means that a large number of transmissions has to be used, which

☆ This work was supported in part by the Swedish Research Council (VR), Carl Trygger's foundation, and the European Research Council (ERC grant agreement numbers 228044 and 247035).

* Corresponding author at: Department of Mathematical Statistics, Lund University, P.O. Box 118, SE-221 00 Lund, Sweden.
E-mail addresses: erikg@maths.lth.se (E. Gudmundson), andreas.jakobsson@matstat.lu.se (A. Jakobsson), jaj@elektro.dtu.dk (J.A. Jensen), ps@it.uu.se (P. Stoica).

0165-1684/$ - see front matter © 2011 Elsevier B.V. All rights reserved.
doi:10.1016/j.sigpro.2010.12.014

reduces the temporal resolution and makes it difficult to see details in the rapid acceleration phases of the cardiac cycle [2]. Furthermore, it is generally also necessary to acquire B-mode images, allowing the operator to navigate and choose the region in which the blood velocity should be estimated. As the same system is used for both the velocity estimation and for forming B-mode images, these two transmissions are interleaved. Since it is desirable to update the B-mode images frequently to allow the operator to find and track the vessel position, it is necessary to reduce the number of Doppler transmissions [1].

In [3], the authors introduced the data-adaptive Capon- and APES-based blood velocity spectral estimation techniques, herein termed the *Blood Power spectral Capon* (BPC) and the *Blood APES* (BAPES) techniques. These techniques exploit the availability of additional measurements from neighboring depths to improve the performance of the estimators, as well as make use of the recent development in high-resolution data-adaptive spectral estimation techniques. A simple reformulation of BPC along the lines of [4] would also allow for an amplitude spectral Capon approach, which we here term the *Blood Capon* (B-Capon) approach. As shown in [3], these methods offer substantial improvements over the traditionally used Welch's method, allowing for an accurate estimation of the blood spectrum using drastically fewer emissions as compared to the Welch's method. These results have also been confirmed in thorough *in vivo* studies [5,6].

Recently, researchers have examined spectral estimation techniques that allow for irregular sampling schemes, so that B-mode images can be acquired in between the regular Doppler transmissions. As it is crucial to maintain the Nyquist frequency, one has to be careful when considering interleaved acquisition techniques. For example, if every second Doppler transmission is replaced by a B-mode image acquisition, the Nyquist limit is halved, reducing the velocity range by a factor of two. In [7], a correlation-based technique for spectral estimation was proposed, allowing for random sampling schemes; however, the method requires large sets of data and in sampling schemes with few Doppler emissions, aliasing occurs. Moreover, in [8], the missing samples, i.e., samples where a B-mode image was acquired instead, were reconstructed using a filter bank technique, so that a spectrogram can be estimated from a full set of data. The technique, however, reduces the velocity range in proportion to the number of missing samples.

Recently, the case of periodically gapped (PG) measurements was investigated in [9], and the B-Capon and BAPES methods were extended along the lines of [10]; these methods are here termed the BPG-Capon and the BPG-APES techniques. However, the methods in [9] are restricted to the case of periodically gapped sampling of the emissions and will not work for more general irregular sampling schemes.

Typically, to allow for an adequate updating frequency of the B-mode images, about 40% of all the transmissions should be the broad-band pulses used to form the B-mode images. Furthermore, it would be beneficial if the remaining measurements could be arranged such that two different regions of interest could be examined simultaneously, for instance, allowing the medical doctor to compare the blood velocities before and after a region of stenosis in the blood vessels [11]. These requirements, along with the desire to be able to form arbitrary sampling patterns, e.g., to allow for more or less detailed estimates in various regions, necessitate the development of improved techniques able to estimate the blood spectral density from arbitrary sampled and often sparse emissions.

In this paper, making use of recent work in MIMO radar systems [12–15], we propose two data-adaptive iterative blood velocity spectral estimators that allow for an arbitrary sampling of the measurement over emissions. Using both simplified and realistic Field II [16] simulation data, as well as *in vivo* data, we show that the presented methods allow for a reliable estimation of the blood velocity spectrum using only 30% of the available measurements, thus allowing for the velocity estimation at two different regions of interest, while still updating the B-mode images at an adequate pace.

The paper is outlined as follows. In the next section, we present the data model and the new algorithms. In Section 3, we show the performance of the proposed algorithms and compare with existing state-of-the-art techniques. Finally, in Section 4, we conclude the paper.

Some words on notation: In the following, $(\cdot)^T$ and $(\cdot)^*$ denote the transpose and the Hermitian, or conjugate transpose, respectively. Moreover, diag($\boldsymbol{x}$), $\boldsymbol{I}_N$, and $[\boldsymbol{X}]_{k,l}$ denote a diagonal matrix formed with the vector $\boldsymbol{x}$ along the diagonal, the identity matrix of size $N \times N$, and the (k,l)-th element of $\boldsymbol{X}$, respectively. Finally, $\|\cdot\|$ denotes the two-norm. Note that the figures in this paper are displayed in color in the online version.

2. Theory and methods

The data acquired by the spectral Doppler at depth k, corresponding to emission n, is commonly modeled as [1,3]

$$x_k(n) = \alpha_{v_z} e^{j\phi k + j\psi_{v_z} n} + w_k(n), \tag{2}$$

where α_{v_z} is the (complex-valued) amplitude of the sinusoidal signal at frequency ψ_{v_z}, which is directly related to the blood velocity v_z as

$$\psi_{v_z} = -\frac{2\omega_c}{cf_{prf}} v_z = -\frac{2v_z}{c}\omega_c T_{prf}, \tag{3}$$

where $\omega_c = 2\pi f_c$, and T_{prf} is the time between pulse repetitions. Furthermore, ϕ is the demodulating frequency, relating the samples at each depth, and defined as

$$\phi = \frac{\omega_c}{f_s}, \tag{4}$$

where f_s is the sampling frequency. $w_{k(n)}$ denotes a residual term consisting of all signals at velocities different from v_z as well as additive noise. From (2) and (3), we see that the PSD with respect to ψ_{v_z} is equivalent to the blood velocity distribution at the examined location, so the problem of estimating the blood velocity can be seen to be equivalent to the estimation of $|\alpha_{v_z}|^2$ for each velocity of interest. We will herein make no assumptions

on the sampling pattern over emissions, nor the sampling along depth, thus allowing for an arbitrary sampling scheme in both domains. The emission times (sometimes also referred to as *slow-time*) are therefore denoted $n=n_1,\ldots,n_N$, and the samples along depth (sometimes also referred to as *fast-time*) $k=k_1,\ldots,k_K$.

We will now rewrite the signal in (2), describing it as the sum of the contributions from each frequency grid point $\{\psi_{m,v_z}\}_{m=1}^{M}$,

$$x_k(n)=e^{j\phi k}\sum_{m=1}^{M}\alpha_{m,v_z}^{(k)}e^{j\psi_{m,v_z}n}+e_k(n), \tag{5}$$

where $n=n_1,\ldots,n_N$ and $e_{k(n)}$ is zero mean white complex Gaussian noise with variance η. This means that any possible noise coloring is modeled by the first term in (5), i.e., the signal part. Due to the smoothness of the blood flow profile, the blood spectral amplitude at various depths, i.e., over a range of depths, $\alpha_{m,v_z}^{(k)}$, $k=k_1,\ldots,k_K$, will be almost constant as long as the range of considered depths is limited to be within the emitted pulse length. Moreover, since ϕ is known, we can proceed to demodulate $x_k(n)$ to simplify the following calculations, introducing

$$z_k(n)=e^{-j\phi k}x_k(n), \tag{6}$$

or, in a more compact form:

$$\boldsymbol{z}_k=\boldsymbol{A}\boldsymbol{\alpha}_{v_z}^{(k)}+\boldsymbol{e}_k, \tag{7}$$

where

$$\boldsymbol{z}_k=[z_k(n_1)\cdots z_k(n_N)]^T, \tag{8}$$

$$\boldsymbol{\alpha}_{v_z}^{(k)}=[\alpha_{1,v_z}^{(k)}\cdots\alpha_{M,v_z}^{(k)}]^T, \tag{9}$$

$$\boldsymbol{A}=[\boldsymbol{a}_1\cdots\boldsymbol{a}_M], \tag{10}$$

$$\boldsymbol{a}_m=[e^{j\psi_{m,v_z}n_1}\ldots e^{j\psi_{m,v_z}n_N}]^T, \tag{11}$$

and where $\boldsymbol{e}_k$ is defined similarly to $\boldsymbol{z}_k$. From the estimate of the amplitudes at depth k, $\hat{\alpha}_{m,v_z}^{(k)}$, one may, due to the smoothness of the blood flow profile, form an estimate of the central amplitude by simply averaging the neighboring amplitude estimates:

$$\hat{\alpha}_{m,v_z}=\frac{1}{K}\sum_{k=k_1}^{k_K}\hat{\alpha}_{m,v_z}^{(k)}. \tag{12}$$

It now remains to find $\hat{\alpha}_{m,v_z}^{(k)}$, $m=1,\ldots,M$, for which we propose two algorithms: the *Blood Iterative Adaptive Approach* (BIAA) algorithm and the *Blood Sparse Learning via Iterative Minimization* (BSLIM) algorithm.

2.1. The BIAA algorithm

Exploiting the similarities to the work in [12–14], we proceed to derive the *Blood Iterative Adaptive Approach* (BIAA) algorithm. Noting that $|\alpha_{m,v_z}^{(k)}|^2$ forms a measure of the blood spectral density at velocity v_z, it is clear that the covariance matrix of the data $\boldsymbol{z}_k$ can be expressed as

$$\boldsymbol{R}_{BIAA}^{(k)}=\sum_{m=1}^{M}|\alpha_{m,v_z}^{(k)}|^2\boldsymbol{a}_m\boldsymbol{a}_m^*+\eta\boldsymbol{I}_N=\boldsymbol{A}\boldsymbol{P}_{BIAA}^{(k)}\boldsymbol{A}^*+\eta\boldsymbol{I}_N, \tag{13}$$

where

$$\boldsymbol{P}_{BIAA}^{(k)}=\mathrm{diag}([p_{BIAA}^{(1,k)}\cdots p_{BIAA}^{(M,k)}]), \tag{14}$$

$$p_{BIAA}^{(m,k)}=|\alpha_{m,v_z}^{(k)}|^2. \tag{15}$$

It should be noted that the amplitudes at neighboring depths are approximately the same, suggesting that one should form the estimate using the mean of the covariance matrices:

$$\boldsymbol{R}_{BIAA}=\frac{1}{K}\sum_{k=k_1}^{k_K}\boldsymbol{R}_{BIAA}^{(k)}=\frac{1}{K}\boldsymbol{A}\left[\sum_{k=k_1}^{k_K}\boldsymbol{P}_{BIAA}^{(k)}\right]\boldsymbol{A}^*+\eta\boldsymbol{I}. \tag{16}$$

The interference covariance matrix, i.e., the contribution from all points on the frequency grid except ψ_{m,v_z}, can now be defined as

$$\boldsymbol{Q}_m=\boldsymbol{R}_{BIAA}-|\alpha_{m,v_z}|^2\boldsymbol{a}_m\boldsymbol{a}_m^*. \tag{17}$$

In order to find an estimate of $\alpha_{m,v_z}^{(k)}$, we consider the general linear estimator

$$\hat{\alpha}_{m,v_z}^{(k)}=\boldsymbol{h}_m^*\boldsymbol{z}_k. \tag{18}$$

Then, the weight vector $\boldsymbol{h}_m$ can be found by solving the following constrained minimization

$$\min_{\boldsymbol{h}_m}\boldsymbol{h}_m^*\boldsymbol{Q}_m\boldsymbol{h}_m\quad\text{s.t.}\quad\boldsymbol{h}_m^*\boldsymbol{a}_m=1, \tag{19}$$

i.e., the mth weight vector is designed as a linear estimator that minimizes the output from all grid points other than ψ_{m,v_z}, while passing the component with the frequency of interest undistorted. As is readily seen, (19) is equivalent to

$$\min_{\boldsymbol{h}_m}\boldsymbol{h}_m^*\underbrace{(\boldsymbol{Q}_m+|\alpha_{m,v_z}|^2\boldsymbol{a}_m\boldsymbol{a}_m^*)}_{\boldsymbol{R}_{BIAA}}\boldsymbol{h}_m\quad\text{s.t.}\quad\boldsymbol{h}_m^*\boldsymbol{a}_m=1, \tag{20}$$

to which the minimizer is found as (see, e.g., [2])

$$\hat{\boldsymbol{h}}_m=\frac{\boldsymbol{R}_{BIAA}^{-1}\boldsymbol{a}_m}{\boldsymbol{a}_m^*\boldsymbol{R}_{BIAA}^{-1}\boldsymbol{a}_m}. \tag{21}$$

An estimate of the amplitude at ψ_{m,v_z} can thus be found by inserting (21) in (18), yielding

$$\hat{\alpha}_{m,v_z}^{(k)}=\frac{\boldsymbol{a}_m^*\boldsymbol{R}_{BIAA}^{-1}\boldsymbol{z}_k}{\boldsymbol{a}_m^*\boldsymbol{R}_{BIAA}^{-1}\boldsymbol{a}_m}, \tag{22}$$

and an estimate over all depths can be found from (12).

It now remains to find an estimate of the noise variance η. Reminiscent of [17], we propose a method that computes the variance for each emission and depth, and then averages these estimates. Let $\eta_{n,k}$ denote the variance of sample k along depth, at emission n. The steering vector corresponding to $\eta_{n,k}^{1/2}$ is then the nth column of $\boldsymbol{I}_N$, here denoted $\boldsymbol{v}_n$. Consequently, an estimate of $\eta_{n,k}$ is given by [17]

$$\hat{\eta}_{n,k}=\left|\frac{\boldsymbol{v}_n^*\boldsymbol{R}_{BIAA}^{-1}\boldsymbol{z}_k}{\boldsymbol{v}_n^*\boldsymbol{R}_{BIAA}^{-1}\boldsymbol{v}_n}\right|^2, \tag{23}$$

and the noise variance estimate can be computed as

$$\hat{\eta}_{BIAA}=\frac{1}{NK}\sum_{n=n_1}^{n_N}\sum_{k=k_1}^{k_K}\hat{\eta}_{n,k}. \tag{24}$$

As $\boldsymbol{R}_{BIAA}$ depends on α_{m,v_z} (or, rather, $\alpha_{m,v_z}^{(k)}$), BIAA must be implemented as an iterative algorithm. Herein, we suggest

Table 1
Outline of the BIAA and BSLIM algorithms ($B_{\cdot}$ denotes BIAA or BSLIM).

	BIAA	BSLIM
Initialize:	$z_k(n)=e^{-j\phi k}x_k(n)$, $\hat{\alpha}^{(k)}_{m,\nu_z}=\boldsymbol{a}_m^*\boldsymbol{z}_k/N$, $\hat{\eta}=10^{-9}$,	
Step 1:	$p^{(m,k)}_{BIAA}=\lvert\hat{\alpha}^{(k)}_{m,\nu_z}\rvert^2$,	$p^{(m,k)}_{BSLIM}=\lvert\hat{\alpha}^{(k)}_{m,\nu_z}\rvert$,
Step 2:	$\boldsymbol{P}^{(k)}_{B_{\cdot}}=\mathrm{diag}([p^{(1,k)}_{B_{\cdot}}\cdots p^{(M,k)}_{B_{\cdot}}])$, $\boldsymbol{P}_{B_{\cdot}}=\frac{1}{K}\sum_{k=k_1}^{k_K}\boldsymbol{P}^{(k)}_{B_{\cdot}}$, $\boldsymbol{R}_{B_{\cdot}}=\frac{1}{K}\boldsymbol{A}\boldsymbol{P}_{B_{\cdot}}\boldsymbol{A}^*+\hat{\eta}_{B_{\cdot}}\boldsymbol{I}$,	
Step 3:	$\hat{\alpha}^{(k)}_{m,\nu_z}=\frac{\boldsymbol{a}_m^*\boldsymbol{R}^{-1}_{BIAA}\boldsymbol{z}_k}{\boldsymbol{a}_m^*\boldsymbol{R}^{-1}_{BIAA}\boldsymbol{a}_m}$,	$p^{(m)}_{BSLIM}=[\boldsymbol{P}_{BSLIM}]_{m,m}$, $\hat{\alpha}^{(k)}_{m,\nu_z}=p^{(m)}_{BSLIM}\boldsymbol{a}_m^*\boldsymbol{R}^{-1}_{BSLIM}\boldsymbol{z}_k$,
Step 4:	$\hat{\eta}_{n,k}=\left\lvert\frac{\boldsymbol{v}_n^*\boldsymbol{R}^{-1}_{BIAA}\boldsymbol{z}_k}{\boldsymbol{v}_n^*\boldsymbol{R}^{-1}_{BIAA}\boldsymbol{v}_n}\right\rvert^2$, $\hat{\eta}_{BIAA}=\frac{1}{NK}\sum_{n=n_1}^{n_N}\sum_{k=k_1}^{k_K}\hat{\eta}_{n,k}$.	$\hat{\eta}^{(k)}_{BSLIM}=\frac{1}{N}\left\lVert\boldsymbol{z}_k-\boldsymbol{A}\hat{\boldsymbol{\alpha}}^{(k)}_{\nu_z}\right\rVert^2$, $\hat{\eta}_{BSLIM}=\frac{1}{K}\sum_{k=k_1}^{k_K}\hat{\eta}^{(k)}_{BSLIM}$.
Step 5:	Repeat Steps 1–4 until practical convergence.	
Finalize:	$\hat{\alpha}_{m,\nu_z}=\frac{1}{K}\sum_{k=k_1}^{k_K}\hat{\alpha}^{(k)}_{m,\nu_z}$.	

to use the least squares (LS) estimate as initialization for the amplitudes:

$$\hat{\alpha}^{(k)}_{m,\nu_z}=\boldsymbol{a}_m^*\boldsymbol{z}_k/N. \tag{25}$$

The noise variance estimate can be initialized setting it to a small number, e.g., 10^{-9}. The BIAA spectral estimators are thus found by iterating the estimation of $\boldsymbol{R}_{BIAA}$ in (16), and the estimation of the amplitudes in (22), until a suitable stopping criterion is met. The amplitude estimate is then obtained through (12). See Table 1 for an outline of the BIAA algorithm.

Herein, we iterate until the estimates have practically converged, i.e., the difference between the amplitude estimates between two consecutive iterations is smaller than some preset threshold ε, which generally requires no more than 10–15 iterations. We note that in [17], the IAA algorithm has been shown to converge locally. All indications suggest that a similar result would hold also for BIAA.

We also note that it would be possible to form the BIAA amplitude estimate using the mean of the data over the depths, i.e., using $\overline{\boldsymbol{z}}=(1/K)\sum_{k=k_1}^{k_K}\boldsymbol{z}_k$, or by computing the amplitude estimates for depth k using $\boldsymbol{R}^{(k)}_{BIAA}$ and not $\boldsymbol{R}^{(l)}_{BIAA}$, $k\neq l$. However, the latter approach is not recommended as this would require the computation of K covariance matrices together with their inverse. Empirical studies also show that the BIAA algorithm herein proposed outperforms the version using the mean of the data.

2.2. The BSLIM algorithm

We now proceed to examine an alternative iterative approach, termed the *Blood Sparse Learning via Iterative Minimization* (BSLIM) algorithm. Reminiscent of [15], we then instead find an estimate of the amplitudes from the following regularized minimization problem:

$$(\hat{\boldsymbol{\alpha}}^{(k)}_{\nu_z},\hat{\eta})=\min_{\boldsymbol{\alpha}^{(k)}_{\nu_z},\eta}\frac{N}{2}\log\eta+\frac{1}{2\eta}\lVert\boldsymbol{z}_k-\boldsymbol{A}\boldsymbol{\alpha}^{(k)}_{\nu_z}\rVert^2+\sum_{m=1}^{M}\lvert\alpha^{(k)}_{m,\nu_z}\rvert, \tag{26}$$

where the first part of the minimization criterion,

$$\frac{N}{2}\log\eta+\frac{1}{2\eta}\lVert\boldsymbol{z}_k-\boldsymbol{A}\boldsymbol{\alpha}^{(k)}_{\nu_z}\rVert^2, \tag{27}$$

is a quadratic fitting of the model to the data, scaled with the unknown noise variance η. The third term on the other hand, is a regularization term, preventing an overfit of the model to the noisy data. The following iterative algorithm provides a solution to (26)

$$\hat{\alpha}^{(k)}_{m,\nu_z}=p^{(m)}_{BSLIM}\boldsymbol{a}_m^*\boldsymbol{R}^{-1}_{BSLIM}\boldsymbol{z}_k, \tag{28}$$

where

$$\boldsymbol{R}_{BSLIM}=\boldsymbol{A}\boldsymbol{P}_{BSLIM}\boldsymbol{A}^*+\hat{\eta}_{BSLIM}\boldsymbol{I}, \tag{29}$$

$$\boldsymbol{P}_{BSLIM}=\frac{1}{K}\sum_{k=k_1}^{k_K}\boldsymbol{P}^{(k)}_{BSLIM}, \tag{30}$$

$$\boldsymbol{P}^{(k)}_{BSLIM}=\mathrm{diag}([p^{(1,k)}_{BSLIM}\ \cdots\ p^{(M,k)}_{BSLIM}]), \tag{31}$$

$$p^{(m,k)}_{BSLIM}=\lvert\alpha^{(k)}_{m,\nu_z}\rvert, \tag{32}$$

$$\hat{\eta}_{BSLIM}=\frac{1}{K}\sum_{k=k_1}^{k_K}\hat{\eta}^{(k)}_{BSLIM}, \tag{33}$$

$$\hat{\eta}^{(k)}_{BSLIM}=\frac{1}{N}\lVert\boldsymbol{z}_k-\boldsymbol{A}\boldsymbol{\alpha}^{(k)}_{\nu_z}\rVert^2, \tag{34}$$

$$p^{(m)}_{BSLIM}=[\boldsymbol{P}_{BSLIM}]_{m,m}. \tag{35}$$

As $\boldsymbol{P}_{BSLIM}$ depends on the unknown amplitudes, BSLIM is also implemented as an iterative algorithm, initialized similarly to BIAA, i.e., using (25) together with $\eta_0=10^{-9}$. We refer to [15] for a proof of convergence of the SLIM algorithm. All indications suggest that a similar result would hold also for BSLIM. See Table 1 for an outline of the BSLIM algorithm.

We note that, similarly to BIAA, it is possible to compute the amplitude estimates from the mean over the depths, or by computing the amplitudes for depth k using only $\boldsymbol{P}^{(k)}_{BSLIM}$ and $\hat{\eta}^{(k)}_{BSLIM}$. However, these approaches are not recommended for the same reasons as for BIAA.

We also remark that, reminiscent of [15], it would be possible to derive BSLIM algorithms where

$$p^{(m,k)}_{BSLIM}=\lvert\alpha^{(k)}_{m,\nu_z}\rvert^{2-q} \tag{36}$$

for $0<q\leq 1$. However, setting $q<1$ is not recommended as this will provide a sparser solution and the blood velocity is often distributed over a range of velocities, so the peak could be quite broad, especially for higher velocities. Therefore, we propose a BSLIM algorithm where we use $q=1$.

2.3. Comparison of BIAA and BSLIM

In Table 1, the BIAA and BSLIM algorithms are outlined in a way that makes their comparison easier. It is worth noting that the BIAA amplitude estimate in (22) has many similarities with the Capon method (see, e.g., [2]). According to [2], we have

$$p_{BIAA}^{(m,k)} = |\alpha_{m,v_z}^{(k)}|^2 \approx \frac{1}{\boldsymbol{a}_m^* \boldsymbol{R}^{-1} \boldsymbol{a}_m}, \tag{37}$$

so we can rewrite the amplitude estimate in (22) as

$$\hat{\alpha}_{m,v_z}^{(k)} \approx p_{BIAA}^{(m,k)} \boldsymbol{a}_m^* \boldsymbol{R}_{BIAA}^{-1} \boldsymbol{z}_k. \tag{38}$$

We see that the main difference between BIAA and BSLIM therefore lies in the formation of the power matrix, $\boldsymbol{P}$, in the sense that BSLIM is computed from the magnitude of the most recent estimate of the amplitudes, whereas BIAA uses the magnitude squared.

3. Numerical results

We now proceed to evaluating the performance of the proposed algorithms, first by the use of a simplified signal, where the mean squared error (MSE) of the velocity estimate from the different estimation techniques are compared. We define the MSE of an estimate $\hat{x}$ as

$$\mathrm{MSE}(\hat{x}) = E\{(x-\hat{x})^2\}, \tag{39}$$

where $E\{\cdot\}$ is the expectation operator and x denotes the true parameter value. We will evaluate the expression in (39) empirically (200 Monte-Carlo simulations) for different signal-to-noise ratios (SNR's), defined as $\mathrm{SNR} = \sigma_s^2/\eta$, with σ_s^2 denoting the signal energy. We then proceed to a more realistic simulation, examining the same sampling pattern, but where the data is generated using the Field II toolbox [16]. Finally, the methods are evaluated on *in vivo* data. In the following, the spectra for the simplified and Field II simulations are generated using K=33 regularly spaced samples along depth, whereas for the *in vivo* data, K=40. Each power spectrum consists of 500 equally spaced points in the interval $\psi_{v_z} \in [-0.5, 0.5)$.

3.1. Simplified simulations

We generated data using (5) with P=1 sinusoid, having a true velocity of 0.2 m/s and amplitude $\alpha_{v_z} = 1$, and with f_c, f_s, c, and f_{prf} according to Table 2. The data was corrupted by zero mean white Gaussian circularly symmetric noise with variance η. The algorithms were then compared using the MSE of the estimated velocity.

Table 2
Parameters for transducer and femoral flow simulation.

Transducer center frequency	f_c	5 MHz
Pulse cycles	M	4
Speed of sound	c	1540 m/s
Pitch of transducer element	w	0.338 mm
Height of transducer element	h_e	5 mm
Kerf	k_e	0.0308 mm
Number of active elements	N_e	128
Corresponding range gate size		123 mm
Sampling frequency	f_s	20 MHz
Pulse repetition frequency	f_{prf}	15 kHz
Radius of vessel	R	4.2 mm
Distance to vessel center	Z_{ves}	38 mm
Angle between beam and flow		60°

3.1.1. Sampling pattern 1

First, we study the case of 32 regularly spaced samples of data along emissions, where we compare our proposed methods with the filterbank methods BAPES and B-Capon, proposed in [3], using a filter length of 30 samples, and the traditional Welch's method [16]. We see in Fig. 1(a) that BIAA and BSLIM show similar performance, outperforming the other methods for SNR < -10 dB. The BAPES method shows a minor bias in the velocity estimate; this is as is expected since it relies on APES [18].

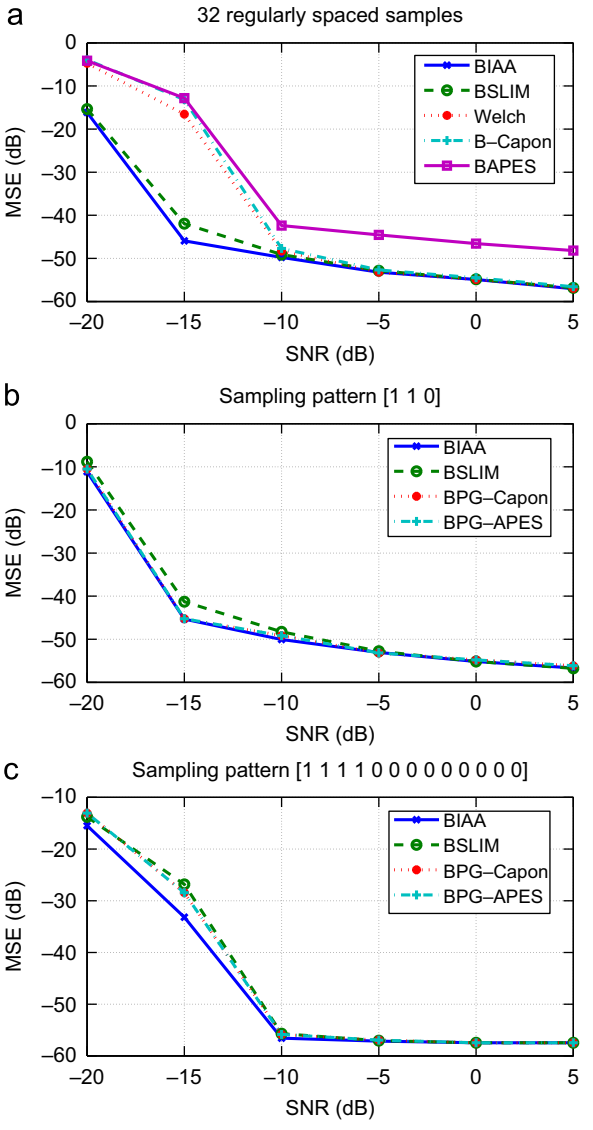

Fig. 1. MSE of velocity estimate in a simplified scenario, with sampling patterns (a) N=32 regularly spaced emissions, (b) 12 blocks of [1 1 0] emissions, and (c) 10 blocks of [1 1 1 1 0 0 0 0 0 0 0 0 0 0] emissions.

3.1.2. Sampling pattern 2

In the second example, we used the sampling scheme [1 1 0] over emissions, where 1 denotes an available sample and 0 that the sample is missing, due to, e.g., B-mode image acquisition. The data was generated using 12 blocks of data, i.e., 36 sampling instances with 24 available samples, with each block containing two available samples and one missing, and we compared the BIAA and BSLIM methods with BPG-Capon and BPG-APES from [9]. For BPG-Capon and BPG-APES, we re-used the settings in [9], i.e., having sample filter length $\tilde{N}_s = 2$ and block filter length $\tilde{N}_c = 2$. For large SNR, all methods perform similarly, but for low SNR, BSLIM is slightly outperformed by the other methods, see Fig. 1(b).

3.1.3. Sampling pattern 3

As a third example, we examined the sampling scheme with pattern [1 1 1 1 0 0 0 0 0 0 0 0 0 0], using ten blocks of data, giving 130 sampling instances with 40 available samples. We again compare BIAA and BSLIM with BPG-Capon and BPG-APES ($\tilde{N}_s = 3$ and $\tilde{N}_c = 5$). With this sampling pattern, it would be possible to use five of the empty sampling instances (38%) to acquire B-mode images, and the remaining four to acquire Doppler transmissions in another region. The result is displayed in Fig. 1(c), where we see that BIAA outperforms the other methods for lower SNR, whereas for higher SNR, all methods perform similarly.

3.2. Femoral artery simulations

To compare the methods in a more realistic scenario, we used the Field II program [16] to generate flow data, using the Womersley model [19] for pulsating flow from the femoral artery. The specific parameters for the flow simulation are summarized in Table 2. As customary, the stationary part of the signal was removed by subtraction of the mean of the signal. For signals taken in regions close to the vessel wall, this stationary part could be very strong, and would, if not removed, easily obstruct the blood velocity signal. Moreover, all spectrograms were produced using a dynamic range of 40 dB. Again, we varied the sampling scheme over emissions between the examples. In Fig. 2, we show a spectrogram generated from the data by the traditional Welch's method (see, e.g., [16,3]), where each vertical line is computed using 130 emissions. This spectrogram can be considered a reference and is what we will compare with in the coming examples.

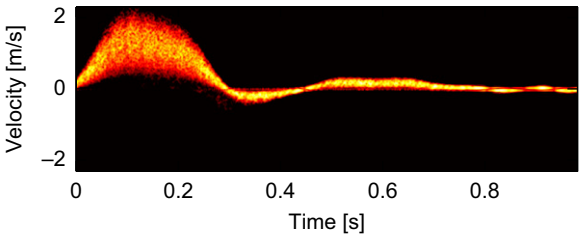

Fig. 2. Traditional spectrogram as reference, created from 130 emissions, averaged over 33 samples along depth.

3.2.1. Sampling pattern 1

Again, we first study the case of 32 regularly spaced emissions. The spectrogram was generated with 16 samples overlap, so half of the samples were reused for the creation of each PSD line. We compared with the filterbank methods BAPES and B-Capon, proposed in [3], using a filter length of 30 samples, as well as the traditional spectrogram [16]. The resulting spectrograms can be seen in Fig. 3. As expected, the traditional spectrogram, computed using Welch's method, shows poor resolution and

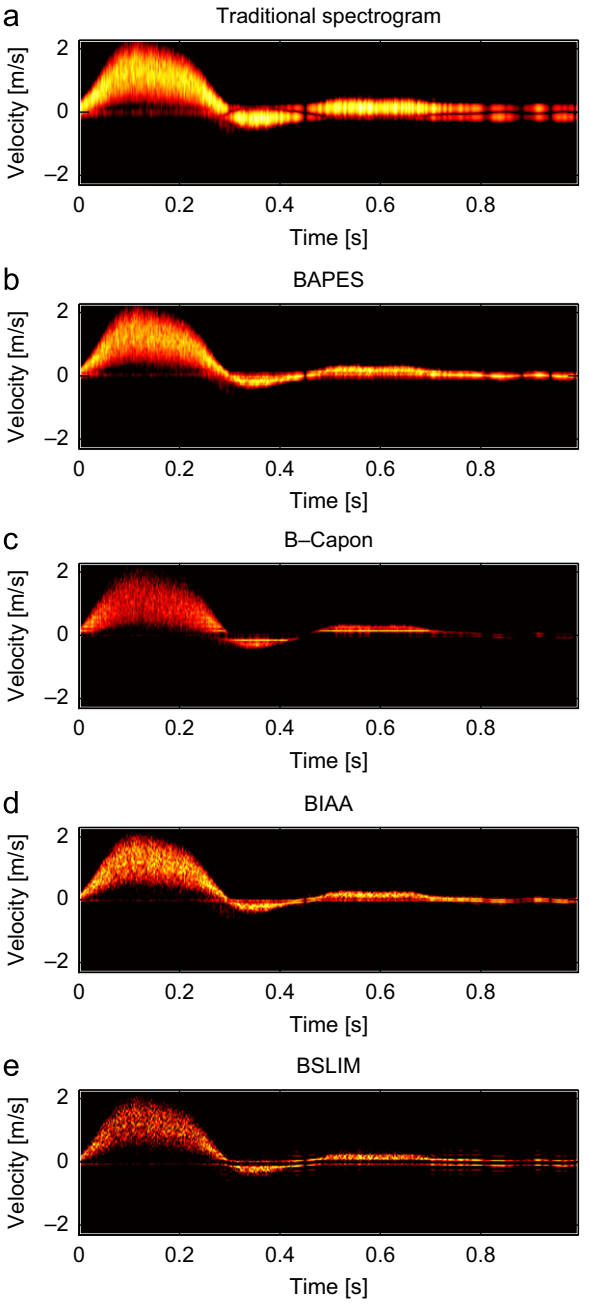

Fig. 3. (a) Traditional spectrogram, (b) BAPES, (c) B-Capon, (d) BIAA, and (e) BSLIM spectrograms, for data consisting of 32 emissions, with 33 samples along depth.

suffers from smearing due to the low number of emissions. Furthermore, BAPES and BIAA show similar performance, with a sharp, clear spectrogram. B-Capon and BSLIM, on the other hand, give estimates that are somewhat blurry, making it harder for the operator to read out the velocity. We also note that the "hole" for velocity 0 that can be seen in the B-Capon, BIAA and BSLIM spectrograms is due to the preprocessing of the signal, where the stationary part was removed.

3.2.2. Sampling pattern 2

In the second example, we compared our proposed methods to the BPG-APES and BPG-Capon methods. The sampling scheme along emissions was [1 1 0] with 12 blocks of data, i.e., 24 available samples were used to create each PSD line in the spectrogram. An overlap of 11 blocks was used, so only one block was new for each PSD line. The resulting spectrograms can be seen in Fig. 4, where we see that both BIAA and BSLIM provide good spectrograms with fewer artifacts as compared to BPG-APES and BPG-Capon. We note that, as a result of the sampling scheme, a velocity component in the interval from 0.06 to 0.22 s has been folded to a negative velocity. Such folding effects may occur for particular sampling schemes, as can also be seen in the examples in the following section.

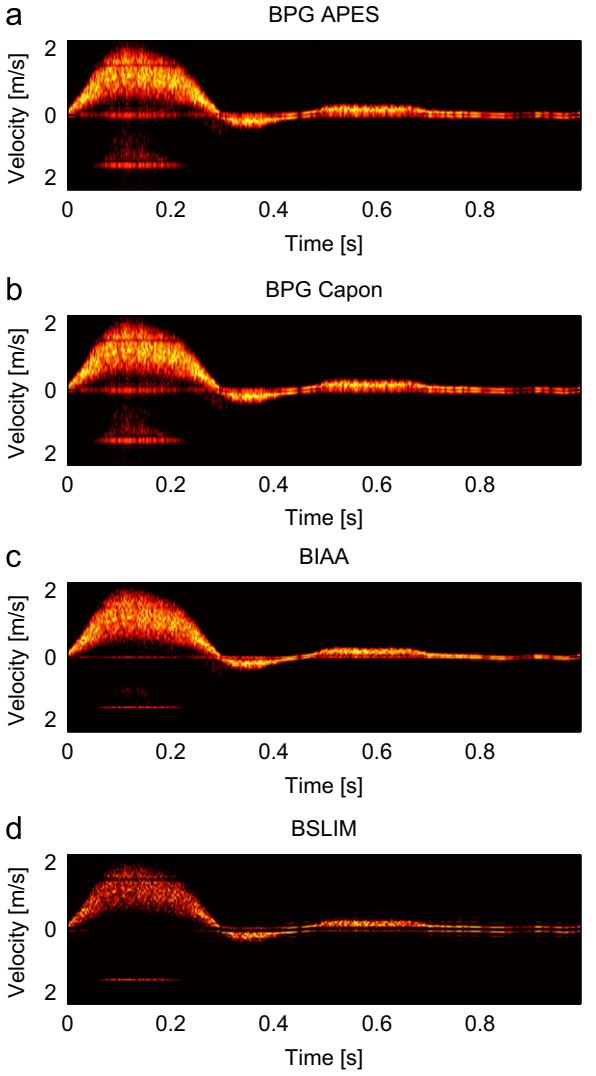

Fig. 4. (a) BPG-APES, (b) BPG-Capon, (c) BIAA, and (d) BSLIM spectrograms, for data consisting of 12 blocks, each with emission pattern [1 1 0], with 33 samples along depth.

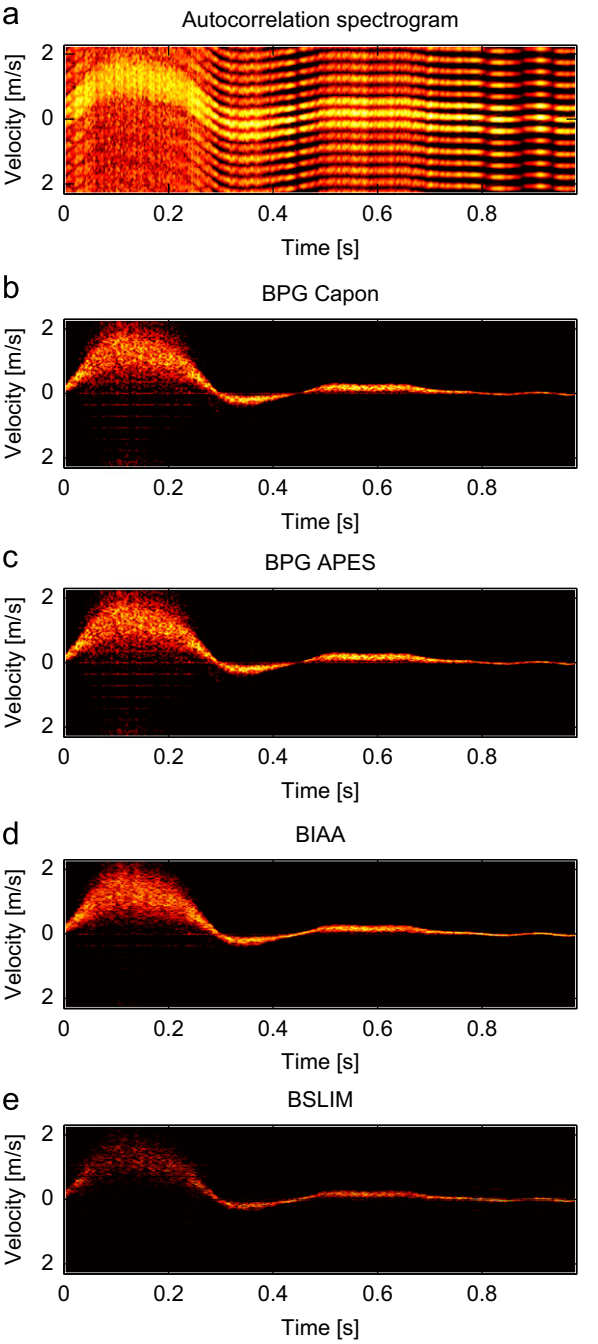

Fig. 5. (a) Autocorrelation spectrogram, (b) BPG-Capon, (c) BPG-APES, (d) BIAA and (e) BSLIM spectrograms, for data consisting of ten blocks with emission pattern [1 1 1 1 0 0 0 0 0 0 0 0 0 0], with 33 samples along depth.

Table 3
Parameters for the *in vivo* data.

Transducer center frequency	f_c	7 MHz
Number of active elements	N_e	64
Sampling frequency	f_s	40 MHz
Pulse repetition frequency	f_{prf}	9.3 kHz
Apodization in transmit		Uniform
Apodization in receive		Hanning

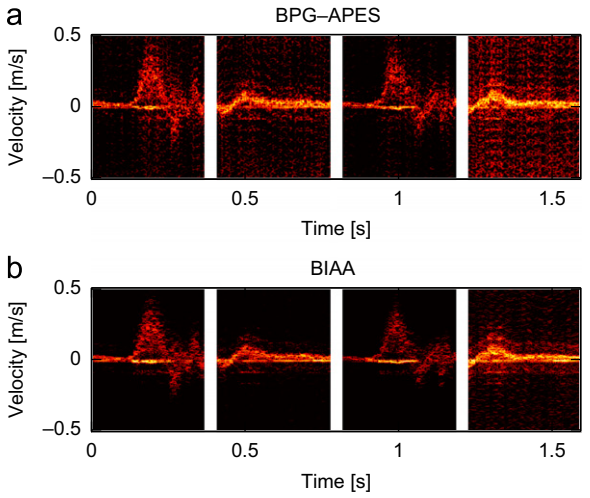

Fig. 6. The (a) BPG-APES and (b) BIAA spectrograms created using ten blocks with emission pattern [1 1 1 1 0 0 0 0 0 0 0 0 0 0], with 40 samples along depth. The strong stationary part of the data covers partly the spectrum.

3.2.3. Sampling pattern 3

Lastly, we compared the spectrograms created for the sampling scheme of pattern [1 1 1 1 0 0 0 0 0 0 0 0 0 0], where ten blocks of data was used per PSD line with nine blocks overlap. As can be seen in Fig. 5, the autocorrelation spectrogram [7] fails for this sampling pattern and BPG-Capon and BPG-APES give significant artifacts in the region of high velocities. BIAA shows less artifacts, still producing a clear spectrogram, closely resembling the reference in Fig. 2. BSLIM shows almost no artifacts but this comes with the cost of not showing such a clear spectrogram as BIAA in the systolic part of the cardiac cycle.

3.3. In vivo data

For a comparison on *in vivo* data, the carotid artery of a healthy volunteer was examined using the experimental scanner RASMUS [20] and a B-K Medical 8804, 7 MHz linear array transducer. This dataset was previously used in [5]; for completeness, the setup is given in Table 3. The stationary part of the signal was removed as detailed in Section 3.2, using mean subtraction. Here, in the interest of brevity, we only examine sampling pattern 3, again using ten blocks of data with nine blocks overlap for each

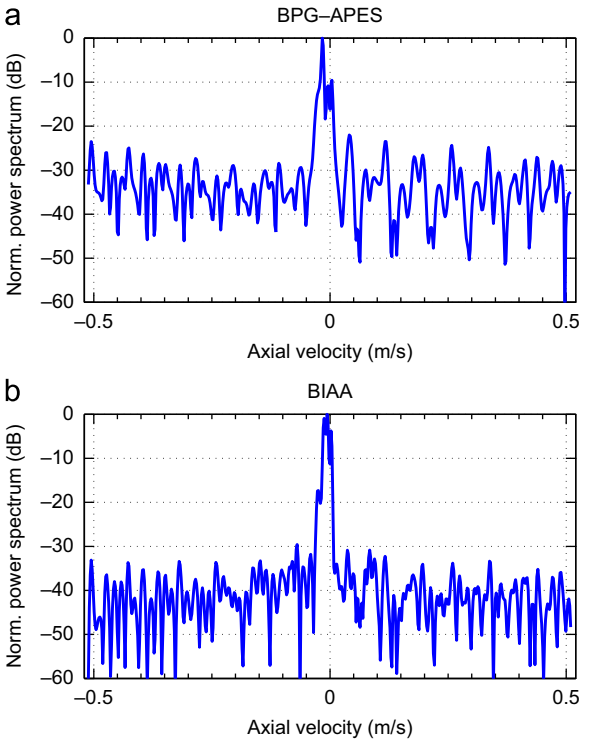

Fig. 7. Spectra from Fig. 6 at time 0.91 s. The width of the main lobes are approximately the same but the BIAA has a lower side lobe level which gives increased contrast.

Table 4
FWHM and contrast for the *in vivo* data.

Method	FWHM (10^{-3} m/s)	Contrast (dB)
BPG-APES	4.2	30
BPG-Capon	4.2	30
BIAA	4.1	37
BSLIM	2.4	51

spectrum. The resulting spectrograms formed by BPG-APES and BIAA are displayed in Fig. 6. The gaps in the spectrograms represent transmissions used for the necessary B-mode images during the data acquisition.[1] As can be expected given the above simulation study, it can be seen that the BPG-APES spectrogram suffers from substantially more artifacts as compared to the BIAA spectrogram. The results using BPG-Capon and BSLIM behave correspondingly, with the latter again yielding somewhat too sparse estimates. Fig. 7 shows the spectra obtained using BPG-APES and BIAA at time 0.91 s, i.e., at end-diastole. As can be seen from the figure, the main lobe is larger and the side lobe level is higher for BPG-APES as

[1] The gaps occur as the dataset was obtained to evaluate the BAPES estimator which requires regular emissions; thus, the B-mode transmissions for this dataset differ from the ones assumed in the here examined example. We remark that if the B-mode emissions are done according to the assumed sampling pattern over emissions, no gaps would occur.

Table 5
Spectral estimation methods and their restrictions.

Method	Reference	Data restrictions
Welch's	[16]	Uniform sampling, long data sequences
Autocorrelation	[7]	Distributed sampling on a uniform or random grid, long data sequences
B-Capon & BAPES	[3]	Uniform sampling
BPG-Capon & BPG-APES	[9]	Block-repetitive sampling on a uniform grid
BIAA & BSLIM		None

compared to BIAA, and we conclude that both the spectral resolution and the contrast are better when using BIAA. The full width at half maximum (FWHM) and the contrast (ratio of main and side lobes), measured according to [5], for the different methods are given in Table 4.

4. Concluding discussion

In this paper, we have proposed two new algorithms for the estimation of blood velocities in medical ultrasound systems. The new algorithms can handle arbitrary sampling schemes of the data, allowing not only for duplex mode where B-mode images are interleaved with the Doppler emissions, but also for modes where two regions of the blood vessels can be interrogated simultaneously, still offering a sufficient B-mode frame rate. In such scenarios, using realistic Field II data, the proposed methods were shown to provide spectrograms containing fewer artifacts than the current state-of-the-art techniques. Simplified MSE simulations also confirmed the accuracy of the BIAA and BSLIM algorithms. Moreover, in MSE simulations, we have shown that in a scenario with 32 regularly spaced samples, the proposed methods are more accurate than the current state-of-the-art techniques. These results were also verified on realistic Field II simulations and using *in vivo* measurements. Finally, in Table 5, we have summarized the possible restrictions on the sampling patterns for the methods that we have used in this paper.

Acknowledgments

Some of the computations were performed using UPPMAX resources under Project p2007002. The authors would like to thank Mr P. Babu and Dr K. Pelckmanns for useful discussions about parameter estimation of sparse signals, Dr I. K. Holfort and Dr F. Gran for access to the *in vivo* data and for helpful discussions.

References

[1] J.A. Jensen, Estimation of Blood Velocities Using Ultrasound, Cambridge University Press, New York, 1996.
[2] P. Stoica, R. Moses, Spectral Analysis of Signals, Prentice Hall, Upper Saddle River, N.J, 2005.
[3] F. Gran, A. Jakobsson, J.A. Jensen, Adaptive spectral doppler estimation, IEEE Transactions on Ultrasonics, Ferroelectrics and Frequency Control 56 (4) (2009) 700–714, doi:10.1109/TUFFC.2009.1093.
[4] P. Stoica, A. Jakobsson, J. Li, Matched-filterbank interpretation of some spectral estimators, Signal Processing 66 (1) (1998) 45–59.
[5] K.L. Hansen, F. Gran, M.M. Pedersen, I.K. Holfort, J.A. Jensen, M.B. Nielsen, In-vivo validation of fast spectral velocity estimation techniques, Ultrasonics 50 (1) (2010) 52–59, doi:10.1016/j.ultras.2009.07.007.
[6] F. Gran, A. Jakobsson, J. Udesen, J.A. Jensen, Fast spectral velocity estimation using adaptive techniques: in-vivo results, in: IEEE Ultrasonics Symposium, 2007, pp. 993–996, doi:10.1109/ULTSYM.2007.253.
[7] J.A. Jensen, Spectral velocity estimation in ultrasound using sparse datasets, Journal of Acoustical Society of America 120 (1) (2006) 211–220.
[8] S. Klingenberg Møllenbach, J.A. Jensen, Duplex scanning using sparse data sequences, in: 2008 IEEE International Ultrasonics Symposium (IUS), 2008, pp. 5–8, doi:10.1109/ULTSYM.2008.0002.
[9] P. Liu, D. Liu, Periodically gapped data spectral velocity estimation in medical ultrasound using spatial and temporal dimensions, in: Proceedings of the 34th IEEE International Conference on Acoustics, Speech, and Signal Processing (ICASSP), 2009, pp. 437–440, doi:10.1109/ICASSP.2009.4959614.
[10] E.G. Larsson, J. Li, Spectral analysis of periodically gapped data, IEEE Transactions on Aerospace and Electronic Systems 39 (3) (2003) 1089–1097, doi:10.1109/TAES.2003.1238761.
[11] N. Oddershede, F. Gran, J.A. Jensen, Multi-frequency encoding for fast color flow or quadroplex imaging, IEEE Transactions on Ultrasonics, Ferroelectrics, and Frequency Control 55 (4) (2008) 778–786, doi:10.1109/TUFFC.2008.712.
[12] T. Yardibi, J. Li, P. Stoica, M. Xue, A.B. Baggeroer, Source localization and sensing: a nonparametric iterative approach based on weighted least squares, IEEE Transactions on Aerospace and Electronic Systems 46 (1) (2010) 425–443.
[13] P. Stoica, J. Li, J. Ling, Missing data recovery via a nonparametric iterative adaptive approach, IEEE Signal Processing Letters 16 (4) (2009) 241–244, doi:10.1109/LSP.2009.2014114.
[14] E. Gudmundson, P. Stoica, J. Li, A. Jakobsson, M.D. Rowe, J.A.S. Smith, J. Ling, Spectral estimation of irregularly sampled exponentially decaying signals with applications to RF spectroscopy, Journal of Magnetic Resonance 203 (1) (2010) 167–176, doi:10.1016/j.jmr.2009.12.015.
[15] X. Tan, W. Roberts, J. Li, P. Stoica, MIMO radar imaging via SLIM, IEEE Transactions on Signal Processing, submitted for publication, available online 〈http://www.it.uu.se/katalog/praba420/SLIM.pdf〉.
[16] J.A. Jensen, N.B. Svendsen, Calculation of pressure fields from arbitrarily shaped, apodized, and excited ultrasound transducers, IEEE Transactions on Ultrasonics, Ferroelectrics and Frequency Control 39 (1992) 262–267.
[17] W. Roberts, P. Stoica, J. Li, T. Yardibi, F.A. Sadjadi, Iterative adaptive approaches to MIMO radar imaging, IEEE Journal of Selected Topics in Signal Processing 4 (1) (2010) 5–20, doi:10.1109/JSTSP.2009.2038964.
[18] A. Jakobsson, P. Stoica, Combining capon and APES for estimation of spectral lines, Circuits, Systems, and Signal Processing 19 (2) (2000) 159–169.
[19] J.R. Womersley, Oscillatory motion of a viscous liquid in a thin-walled elastic tube. I: The linear approximation for long waves, Philosophical Magazine 46 (1955) 199–221.
[20] J.A. Jensen, O. Holm, L.J. Jerisen, H. Bendsen, S.I. Nikolov, B.G. Tomov, P. Munk, M. Hansen, K. Salomonsen, J. Hansen, K. Gormsen, H.M. Pedersen, K.L. Gammelmark, Ultrasound research scanner for real-time synthetic aperture data acquisition, IEEE Transactions on Ultrasonics, Ferroelectrics and Frequency Control 52 (5) (2005) 881–891, doi:10.1109/TUFFC.2005.1503974.